

## **Final Report**

Grant Award Numbers: G15AP00070

Title: Statistical discrimination of induced and tectonic earthquake sequences in Central and Eastern US based on waveform detected catalogs

Investigators: Zhigang Peng  
Georgia Institute of Technology  
311 Ferst Drive  
Atlanta, GA, 30332-0340  
Phone: (404) 894-0231, Fax: (404) 894-5638  
zpeng@gatech.edu

Term Covered by the Report: May 2015 - April 2016 (No cost extension to April 2017)

Funding amount \$70,000

## 1. Background

Since 2008 there have been many moderate size (i.e.  $4 < M < 6$ ) earthquakes occurred in Central and Eastern US (CEUS), a significant increase comparing to previous decades [Ellsworth, 2013]. It is widely speculated that rapid growing of anthropogenic activities, especially extraction of fossil fuels and disposal of waste fluids, are the primary cause for such an increase in the CEUS. Earthquakes that related to anthropogenic activities are termed as induced earthquakes, which is different from naturally occurring earthquakes driven by tectonic forces. Many studies have investigated the connection between anthropogenic activities (i.e., hydraulic fracturing and disposal of waste waters) and moderate size earthquakes in CEUS by looking at the temporal and/or spatial relationship between them [e.g. Frohlich, 2012; Horton, 2012; Keranen et al., 2014; Weingarten et al., 2015; Walsh and Zoback, 2015]. Their results have shown that in most cases waste-water disposal is the primary cause of such increases in moderate-size earthquakes in CEUS. In a few isolated regions hydraulic fracturing is also responsible for inducing moderate-size earthquakes [Skoumal et al., 2015]. This is quite different in western Canada and southwest China, where recent studies have shown that hydraulic fracturing operation is the primary cause of moderate-size earthquakes in these regions [Atkinson et al., 2016; Bao and Eaton, 2016; Lei et al., 2017].

This conclusion also invokes questions on the physics underneath of the nucleation of induced earthquakes. In particular, do induced and tectonic earthquake sequences in CEUS share the same statistics, for example the Omori's law [Utsu et al., 1995] and the Gutenberg-Richter's law? A comprehensive comparison of the spatio-temporal evolution pattern and magnitude-frequency distribution between induced and naturally occurring earthquake sequences may greatly improve our understanding on their potential differences. In particular, Llenos and Michael [2013] have shown that it is possible to detect background rate changes and aftershock productivity for sequences in Oklahoma and Arkansas by stochastic epidemic-type aftershock sequence models and statistical tests. However, due to sparse seismic station coverage, the earthquake catalogs in CEUS generally have a magnitude completeness of 2.5 to 3, which means that many smaller magnitude events are missing in the regional or national earthquake catalog.

Recently many groups have utilized the so-called waveform matched filter technique to detect missing small earthquakes for earthquake sequences in Canada [Bao and Eaton, 2016], Illinois [Yang et al., 2009], Ohio [Skoumal et al., 2015] and in Texas, Oklahoma and Colorado [van Der Elst et al., 2013; Chen et al., 2017]. These studies showed that it is possible to identify a few to a few ten times more events that listed in existing catalog. These newly detected events can be used to improve our understanding of the spatio-temporal evolution of each sequence, as well as its relationship with injection parameters.

In the following sections we briefly describe what we have done in the past two years by applying the matched filter method to earthquake sequences in CEUS, including both natural events (i.e., 2011 M5.8 Virginia and the 2014 M4.1 South Carolina earthquakes) and possible induced events in Oklahoma and nearby states.

## 2. Systematic Detections of Microseismicity Following the 2014 M4.1 South Carolina Earthquake [Daniels et al., in prep]

The border between Georgia and South Carolina does not have a high level of seismicity, so the magnitude 4.1 earthquake on February 15, 2014 near Edgefield, SC provides an opportunity to study the distribution of events in this region (Figure 1). The ANSS catalog also records a magnitude 3.0 aftershock, but no other events in are recorded in this sequence. The Savannah river area, which is along the border between Georgia and South Carolina, does not have a high level of seismicity, so this sequence provides an great opportunity to study seismotectonics in this region, and offer a nice comparison with potential induced seismicity in other places.

A waveform matching technique is used to search for missing events between 8 and 22 February 2014. Stations within 100 kilometers of the mainshock are studied, and 9 of these 15

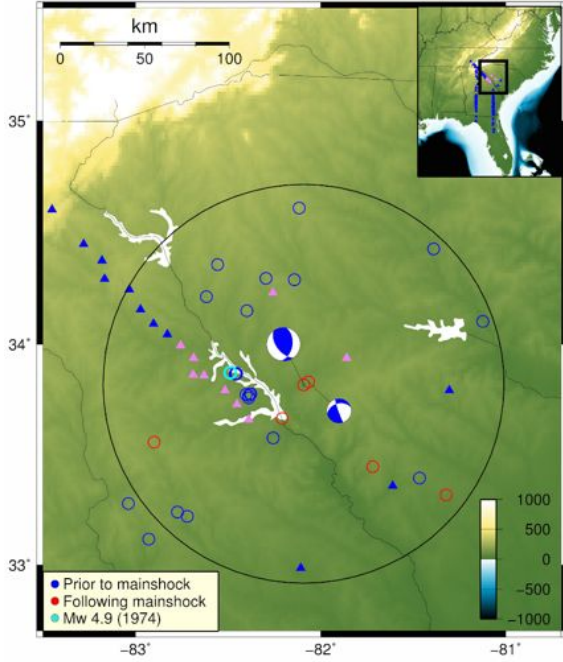


**Fig. 1.** A map of the study region near the border of South Carolina and Georgia. The two beach balls mark the M4.1 mainshock and the M3.0 aftershock. The inset mark the study region in a larger map of CEUS.

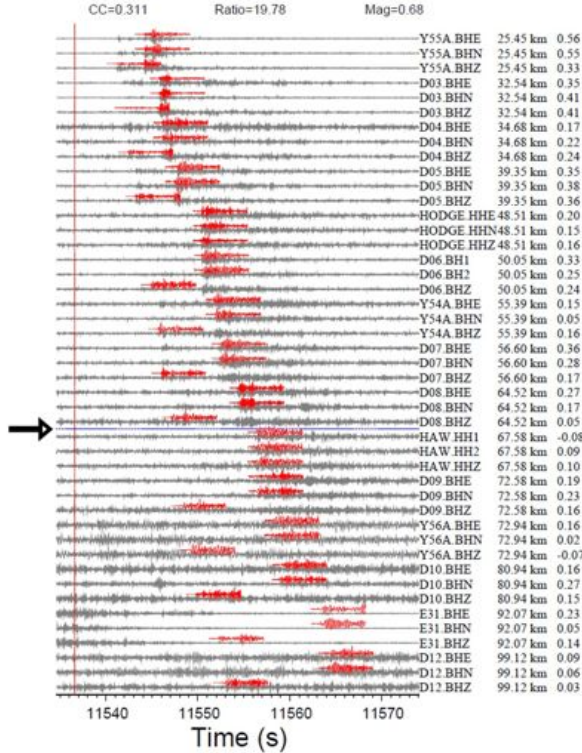


**Fig. 2.** Example of a detected foreshock (gray) using the magnitude 4.1 mainshock waveform as template (red).

stations with the clearest event arrivals are used as part of the final dataset for stacking cross-correlation waveforms. The two ANSS events—the mainshock and recorded aftershock—are used as templates to scan the continuous data for events with similar waveforms. We first filter the data between 2-16 Hz to continuous waveform data between 8<sup>th</sup> and 22<sup>nd</sup> of February 2014. We manually pick the P and S arrivals at stations that recorded both template events.

Signal-to-noise (SNR) ratios are computed for each template waveform. The signal window chosen is 1 second before to 5 seconds after the P and S wave arrival. The noise window is 7 seconds before to 1 second after the P and S wave arrival. Signals with SNR less than 5 are not used in computing cross-correlation (CC) waveforms. Templates with less than 12 channels with an SNR greater than 5 are not used either. The time step—or offset—for computing a CC is set as 0.025 s, and the time window is set to 1 second before to 5 seconds after the arrival time. Of the stations situated within 100 kilometers of the mainshock, nine with the clearest event arrivals are compiled for stacking cross-correlation waveforms. Individual CC waveforms for each day are stacked, resulting in one cross-correlation waveform for each continuous day. The initial detection threshold value is equal to the median plus nine times the median absolute deviation of the signal.

To avoid over-counting events, duplicate detections are removed. If there are multiple detections within two seconds of one another, only the detection with the highest cc value is kept. The remaining events are listed as detections. To obtain an approximation of the magnitude of the detected events, the peak amplitude ratio between waveforms corresponding to the same station is calculated. Figure 2 shows an example of a newly detected magnitude 0.68 event occurred about 11.3 min (682 s) before the mainshock. The mean CC value is 0.311, well above the detection threshold.

As relatively few events are detected with the first two templates, the detections are used in turn as new templates. The same matched filter method is used with the new templates.

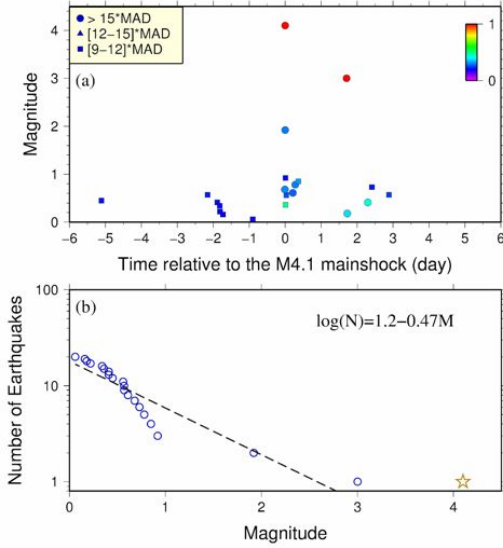


**Fig. 3.** (a) Magnitude versus time of the newly detected events color-coded by the mean CC values. (b) Frequency-magnitude distribution of this sequence.

also 11 aftershock detections, not including the mainshock and Mw 3.0 event. 4 of these events are aftershocks of the Mw 3.0 event, but most of the aftershocks occur on the same day as the mainshock. As shown Figure 3a, several of the aftershocks are detected with the highest threshold of 15 times the MAD, which suggests many can be identified as events with a high amount of confidence. Two of the aftershocks of the Mw 3.0 event have two of the highest cross-correlation coefficients among all detections despite their low magnitudes, which is further evidence that these may be true events.

Overall there are not many detected aftershocks for this event. As Figure 9 demonstrates, the detected number of events falls short of the expected number of events, according to the Båth and Gutenberg-Richter Law [Shcherbakov et al., 2005]. In total there are only 20 detected events—excluding the mainshock—whereas theoretically, upwards of 1000 events would be expected. It is still not clear why this sequence has so few aftershocks as compared with the general statistics.

### 3. On-fault and Off-fault Aftershock Triggering Following the 2011 $M_w$ 5.7 Virginia Earthquake [Meng et al., submitted]

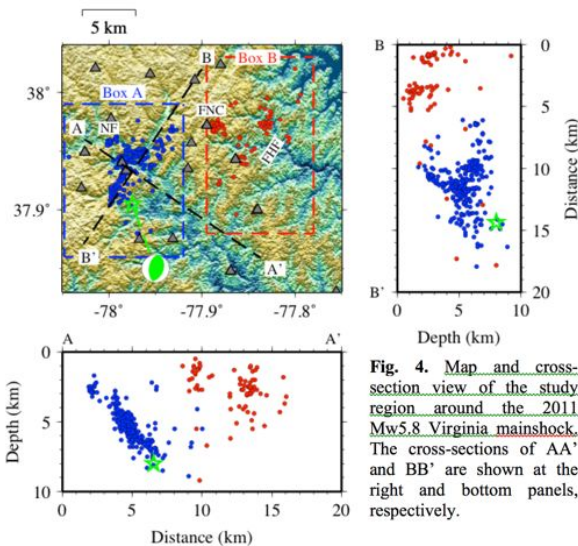


**Fig. 4.** Map and cross-section view of the study region around the 2011 Mw5.8 Virginia mainshock. The cross-sections of AA' and BB' are shown at the right and bottom panels, respectively.

Between the first and new set of detections, if any events occur within a two second window, the event with the larger cross-correlation value is used in the final detection set. Upon stacking cross-correlation waveforms corresponding to the final dataset and running final detections, there are 6 events found using the first two templates—the two ANSS events excluded—as well as 13 events found using the detections as templates, for a total of 19 detections (Figure 3). As shown in Figure 3a, seven of the eight foreshocks are considered as detections only if the threshold is equal to between 9 and 12 times the MAD added to the median. This suggests that, were a higher threshold to be chosen, that most of the potential foreshocks would not be considered detections. Compared to the waveforms

of the Mw 0.68 foreshock in Figure 2, it is debatable as to whether several of the other foreshock waveforms contain true events.

Using the 9 times MAD threshold, there are

#### 3.1 Introduction

At 17:51:05 08/23/2011, an  $M_w$  5.7 earthquake struck Louisa County, Virginia (Figure 4). The mainshock ruptured a shallow, reverse fault striking N29°E and dipping S51°E in the central Virginia seismic zone (CVSZ) [Chapman, 2013]. When the Virginia mainshock occurred, only one permanent broadband seismic station (US.CBN) and a few stations from the Virginia Tech Seismological Observatory (VTSO) were operating within 100 km (Figure 4). To capture the aftershock sequence, 27 temporary seismic stations from 4 different networks were deployed around the epicenter between

~1.5 and 6 days following the mainshock [Chapman, 2013; McNamara et al., 2014]. Because of the prompt and dense installation of seismic instruments, the detailed characteristics of this aftershock sequence have been well studied. In particular, 80 early aftershocks (up to 09/02/2011) are identified and located, using one temporary seismic network [Chapman, 2013]. Moreover, 380 aftershocks are identified and located using four temporary networks from 08/25/2011 to 05/02/2012 by McNamara et al. [2014]. Most aftershocks delineated a fault plane that was consistent with the focal mechanism of the mainshock (Box A in Figure 4). In addition, some aftershocks were northeast to the mainshock's rupture plane and shallower than 5 km (Box B in Figure 4), which were clearly not on the mainshock's rupture plane. Wu et al. [2015] performed aftershock detection using all temporary stations using a combined method of STA/LTA and cross-correlation. Then, they hand-picked arrival times for the detected aftershocks and relocated 1666 events using hypoDD [Waldhauser and Ellsworth, 2000]. They also obtained focal mechanism solutions for 393 aftershocks, which were dominated by reverse faulting.

The 2011 Virginia earthquake sequence and subsequent dense instrumentation provide us a rare opportunity to investigate in details how microseismicity and stress state evolves before and after a moderate-size intraplate earthquake. Studies on earthquake triggering require a high-quality earthquake catalog, which can be obtained via waveform-based matched filter technique [e.g., Peng and Zhao, 2009; Yang et al., 2009; Meng and Peng, 2014]. In this study, we first apply this method to obtain a much more complete catalog around the origin time of the 2011 Virginia earthquake. Then, taking advantage of the massive amount of cross-correlations done during detection, we perform magnitude calibration and hypoDD relocations for the detected aftershocks [e.g., Shelly et al., 2016]. Finally, based on the enhanced catalogs, we analyze both foreshock/aftershock activities, detailed spatial variations of Gutenberg-Richter relationship, aftershock migration and triggering relationship with the Virginia mainshock and hurricane Irene.

### 3.2. Data and Method

We perform matched filter detections between 08/25/2011 00:00:00 and 12/01/2011 00:00:00 using all permanent and temporary stations (Figure 4). The procedure generally follows that of Meng and Peng [2014] and is briefly described below. We use the 380 aftershocks from McNamara et al. [2014] as templates. The arrival times are predicted with a three-layer local velocity model [Chapman, 2013] and software COMLOC [Lin and Shearer, 2006]. We use signal windows 1s before to 4s after both *P*- and *S*-waves on the vertical and horizontal channels

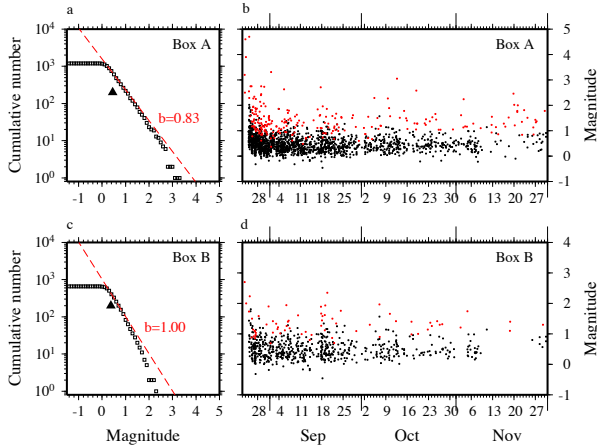


**Fig. 5.** (a) Magnitude-frequency relationship for events in Box A from the detected catalog. The black triangle denotes the  $M_c$ . The red dashed line denotes the best-fitting Gutenberg-Richter relationship. (b) Magnitude versus origin time for the detected (black) and templates (red). (c) and (d) The same plots for events in Box B.

to cross-correlate with the continuous data. Then, all correlation traces from one template are stacked to obtain the mean correlation trace. An event is detected when the mean correlation-coefficient (CC) exceeds the sum of the median value and 9 times the median absolute deviation (MAD) of the mean correlation trace. We then remove all ‘duplicate detections’ if their detecting time windows overlap [Meng et al., 2013a].

Following the detection, we calibrate the relative moment magnitudes of all earthquakes by accurately measuring amplitude ratios between each pair of earthquakes [Cleveland and Ammon, 2015; Shelly et al., 2016]. In addition, as cross-correlation between all pairs of earthquakes are already done, we can conveniently



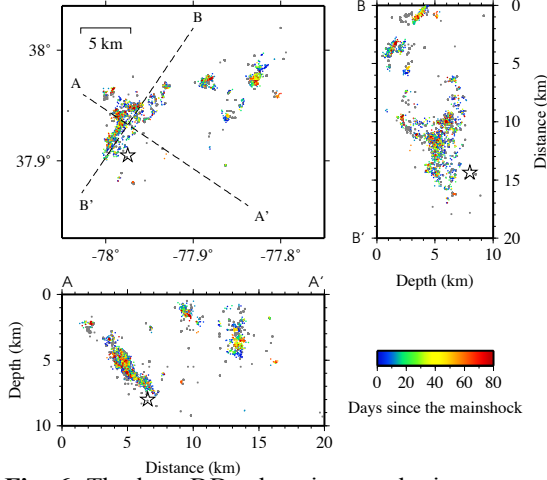


**Fig. 6.** The hypoDD relocation results in map and cross-section view. The star denotes the Virginia mainshock. The grey dots denote templates. The relocated events are color-coded by their origin times.

[Wiemer, 2001] (Figure 5a). For Box B, the  $M_c$  and b-value are 0.37 and 1.00, respectively (Figure 5c).

The hypoDD relocated seismicity generally shows a similar pattern to that from McNamara et al. [2014] and Wu et al. [2015] (Figure 6). In Box A, majority of aftershocks depict a fault plane that strikes  $N34^\circ E$  and dips  $52^\circ SE$ , which is consistent with the focal mechanism solution of the mainshock [Herrmann, 2011]. A cluster of shallow earthquakes was located northwest to the mainshock's rupture planes, which are termed as Northwest Fault (NF) by Horton et al. [2015]. Horton et al. [2015] suggested that aftershocks in Box B can be further divided into two clusters: 1) a tight, shallow cluster of aftershocks (i.e., Fault Northeast of Cuckoo or FNC); 2) a cluster of aftershocks striking NE and dipping vertical (i.e., Fredericks Hall Fault or FHF) (Figure 4). However, our relocation results show that both clusters can be best characterized by fault planes striking NW and dipping NE (Figure 6), consistent with the pattern obtained by Wu et al. [2015]. Moreover, focal mechanisms from these two clusters agree with a NNW striking fault plane [Wu et al., 2015].

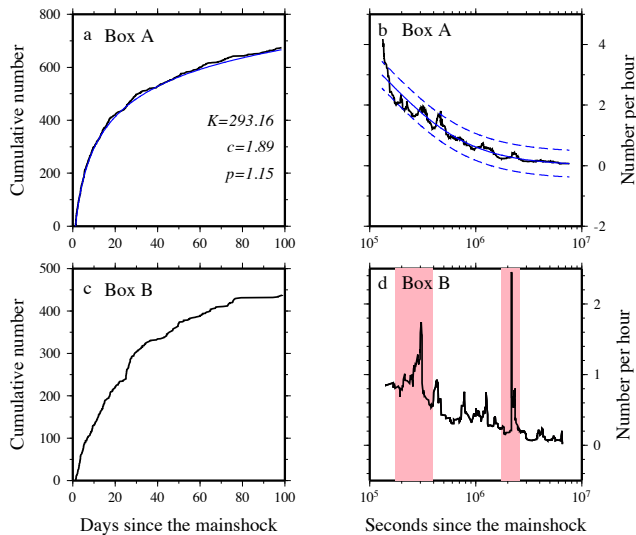


**Fig. 7.** Cumulative number of aftershocks in boxes A (a) and B (c). The corresponding seismicity rate decay in boxes A (b) and B (d). The pink shaded areas are two swarm periods.

extract the correlation-derived differential travel times, following the procedure in Shelly et al. [2016]. The differential travel times are then used to precisely relocate all earthquakes in the software hypoDD [Waldhauser and Ellsworth, 2000].

### 3.3. Aftershock Detection of aftershocks with Temporary Stations

After matched filter detection, magnitude calibration and hypoDD relocation, we obtain 1859 well-constrained earthquakes between 08/25/2011 and 11/30/2011 (hereafter referred as the detected catalog) (Figure 5). Because of the dense temporary networks, we are able to recover aftershocks as small as magnitude  $-0.5$ . For seismicity in Box A, the magnitude of completeness ( $M_c$ ) and b-value are 0.45 and 0.83, respectively, which are obtained by the best-combined method in the software ZMAP

### 3.4. Statistical Behavior of Detected Aftershock Sequences

Next we examine statistical behaviors of newly detected aftershock sequences. In Box A, aftershocks above the  $M_c$  showed a typical Omori decay [Utsu et al., 1995] (Figure 6a and 6b). We fit the seismicity rate changes in Box A with the modified Omori's law using the software Aftpoi [Ogata, 2006]. The best-fitting p-value is 1.15, which is close to that of a typical aftershock sequence (i.e.,  $p=1$ ).

Although the seismicity in Box B gradually decayed with time (Figure 7c and 7d), the rate changes can not be fitted with the

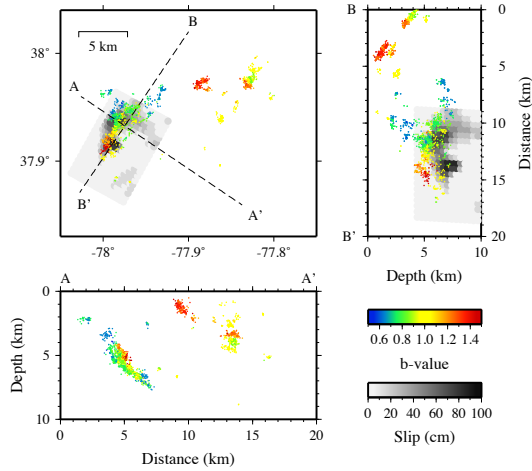


**Fig. 8.** The  $b$ -value map. Each earthquake is color-coded by the  $b$ -value computed from 100 nearest neighbors. The background contour denotes the finite slip model from Hartzell *et al.*, [2013].

section B) of the mainshock's rupture plane. In Box B, most  $b$ -value measurements are larger than 1.0.

It is commonly proposed that  $b$ -value from the Gutenberg-Richter magnitude-frequency relationship increases with decreasing differential stress level [Scholz, 1968]. Schorlemmer *et al.* [2005] found that thrust faulting events, which are under higher stress regime, tend to have lower  $b$ -values than normal faulting events, which are under lower stress regime. Moreover, there was clear correlation between low  $b$ -values obtained from earthquakes prior to the 2011 Tohoku-Oki earthquake and area with high slip during the mainshock, as well as  $b$ -values increment after the mainshock and high slip [Tormann *et al.*, 2015]. For intraplate seismicity, the typical  $b$ -value is around 0.8, lower than the global average of 1.0. The low  $b$ -value could be an indication that intraplate faults are critically stressed due to long recurrence time. Here we found that the  $b$ -values are  $\sim 0.83$  and 1 in Boxes A and B, respectively. However, the  $b$ -value map (Figure 8) also showed clear spatial variations. It is interesting to note that the high  $b$ -values seismicity at the southwestern end located close to areas with little slip (*i.e.*, low stress level) [Hartzell *et al.*, 2013] and the low  $b$ -values seismicity at the northeastern end overlapped with a major slip patch (*i.e.*, high stress level). The overall higher  $b$ -values in Box B indicate relatively low differential stress level, which is consistent with their shallow depths and the occurrences of two swarms possibly related to high fluid pressures. Moreover,  $b$ -values may correlate with material heterogeneity [Mogi, 1962]. Areas with high material heterogeneity are less likely to host large earthquakes because the cracks are small and oriented in all directions, therefore have high  $b$ -values. In summary, the great spatial variability of the  $b$ -values within the Virginia aftershock zone suggests that not all intraplate faults/areas have low  $b$ -values. Instead, it is possible to have very weak or highly fractured area within the overall strong intraplate crust.

### 3.5 Aftershock Triggering Mechanisms

Although earthquakes triggered at remote distances can be only attributed to dynamic stresses, the mechanisms for near-field aftershock triggering (*i.e.*, within one or two rupture lengths) is still elusive [e.g., Felzer and Brodsky, 2006; Richards-Dinger *et al.*, 2010]. Different earthquake triggering mechanisms, including dynamic triggering, static triggering and quasi-static triggering [Freed, 2005], have successfully explained the spatial pattern and/or temporal

modified Omori's law, mainly because of two time periods with elevated seismicity rate (Figure 7d). A close examination reveals that the sudden increase in seismicity during the two time periods can be considered as earthquake swarms occurred along the FHF, which refer to sequences with the largest-magnitude event not at the beginning of a sequence and similar magnitudes for all events [Mogi, 1962]. As shown in Figure 5, the overall  $b$ -values in Boxes A and B are quite different. To further quantify this, we obtain a  $b$ -value map by computing the  $b$ -value at each hypocenter with the nearest 100 events using the best combination method in ZMAP (Figure 8). As expected, the  $b$ -value map shows significant spatial variability across the study region. The majority areas in Box A have typical  $b$ -values for intraplate seismicity (*i.e.*,  $\sim 0.8$ ). We also observe a trend of decreasing  $b$ -values from  $\sim 1.4$  at the southwestern end (cross-section B') to  $\sim 0.7$  at the northeastern end (cross-

evolution of seismicity following certain mainshocks. Below we explore possible mechanisms responsible for triggering aftershocks following the Virginia mainshock.

### 3.5.1 Dynamic triggering

Dynamic stresses carried by seismic waves can trigger earthquakes from immediate vicinity to remote distances (i.e., beyond several rupture lengths) [e.g., Hill et al., 1993]. Most reported cases of dynamic triggering are at far-field, because the triggered earthquakes are easier to be identified during the long-duration and low-frequency surface waves. At near field, dynamic triggering is much more difficult to observe, because the wave train is short and the frequency contents of mainshocks' coda waves and triggered earthquakes are very similar. In this study, although only a few regional seismic stations recorded the Virginia mainshock, it is evident that almost all strong local signals immediately after the mainshock are identified by the matched filter detection. In Box A, 6 aftershocks are detected during the mainshock's coda waves (i.e., < 2000s). Later on, aftershocks in Box A located exclusively NE to the mainshock's epicenter (Figure 6), which is consistent with the rupture directivity (i.e., SW to NE). Such asymmetric aftershock distribution has been used as evidence for near-field dynamic triggering due to the focusing of dynamic stresses [e.g., Kilb et al., 2002; Gomberg et al., 2003]. However, in Box B only 1 and 8 earthquakes occurred within 2000s and 1.5 days after the mainshock, respectively.

Also, the seismicity on the FNC and FHF does not lie on the path of rupture directivity. Therefore, dynamic triggering may best explain the asymmetric aftershock distribution in Box A, while the activation of seismicity in Box B does not support the mechanism of dynamic triggering.

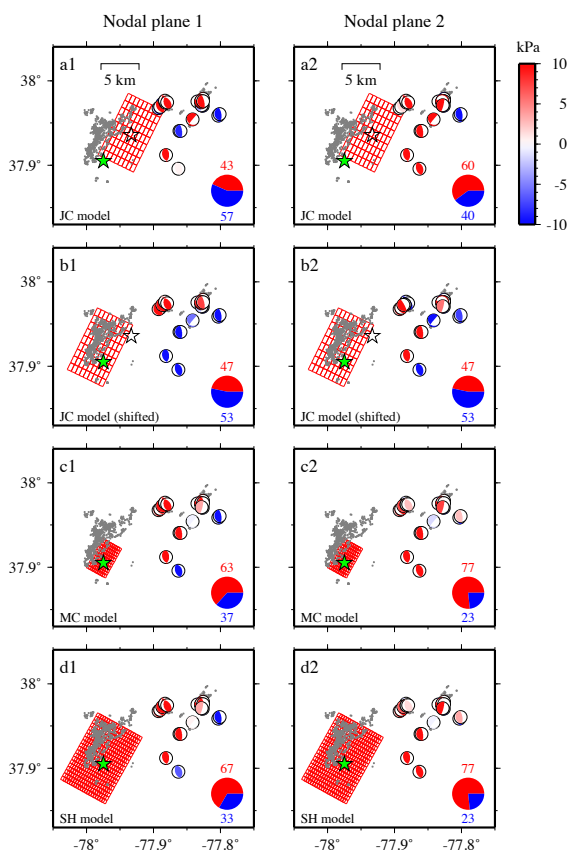


**Fig. 10.** Static Coulomb stress changes using the CJ (a), CJ2 (b), MC (c) and SH model (d). Focal mechanisms are from *Wu et al.*, [2015], which are color-coded by static Coulomb stress changes. The pie chart denotes the percentage of positive and negative static Coulomb stress changes.

### 3.5.2 Static triggering

Static Coulomb stress changes caused by fault displacement are smaller but permanent, comparing to dynamic stress changes. Static triggering could not explain triggering beyond several fault lengths, as static Coulomb stress changes decay very fast with distance [Freed, 2005]. Following the Virginia mainshock, multiple slip models have been obtained. A preliminary slip model was calculated using teleseismic P- and S-waves and the finite fault inverse algorithm [Shao and Ji, 2011] (hereafter referred as the CJ model). However, the CJ model is based on the initial hypocenter reported by United States Geological Survey (USGS) and well separated from the relocated aftershocks (Figure 10a). Similar to Walsh et al. [2015], we shift the CJ model to the relocated hypocenter obtained by Chapman [2013] and refer it as the CJ2 model (Figure 10b). Chapman [2013] proposed a source model based on the location and moment release of three subevents, which is referred as the MC model (Figure 10c). Hartzell et al. [2013] also calculated a finite slip model (the



SH model) using teleseismic P-waves and theoretical Green's functions (Figure 10d).

Walsh et al. [2015] calculated static stress Coulomb changes on the fault planes delineated by aftershocks and known regional fault geometry using the CJ2 model. They concluded that aftershocks along the NF were triggered by the mainshock, while aftershocks at the FNC and FHF were unlikely triggered due to very small Coulomb stress changes. Wu et al. [2015] also conducted static triggering analysis using the MC model and 393 focal mechanism solutions in both boxes. The majority of events had positive Coulomb stress changes no matter which nodal plane was selected. Due to the large variations of fault dimension and slip distribution among four slip models, we compute static Coulomb stress changes using all available slip models to evaluate the model dependency.

It is difficult to obtain accurate static Coulomb stress changes along mainshock's rupture plane, because the heterogeneous slip along the rupture plane is usually unresolvable. Therefore, we only focus on static Coulomb stress changes in Box B, where the Coulomb stress changes are less sensitive to the resolution of slip model. 30 focal mechanism obtained by Wu et al. [2015] showed significant variations in strike, dip and rake (Figure 10). Therefore, assuming a single geometry for receiver faults is not appropriate for static Coulomb stress calculation. Instead, we resolve static Coulomb stress changes on both nodal planes of the 30 focal mechanisms. The results using the CJ and CJ2 models show similar pattern, with ~40-60% of focal mechanisms having positive static Coulomb stress changes on at least one nodal planes. For the MC and SH models, at least 60% of events in Box B are brought closer to failure no matter which nodal plane is used. Although less than half of focal mechanisms have positive Coulomb stress changes using the CJ and CJ2 model, the net seismicity rate may still increase significantly, because seismicity rate decrease is bounded by 0, while seismicity rate increase is unbounded [Toda et al., 2012]. Regardless of slip models, our results suggest that static Coulomb stress changes could explain aftershock triggering in Box B.

### 3.5.3 Afterslip

Afterslip following large earthquakes can be identified by geodetic measurements. However,

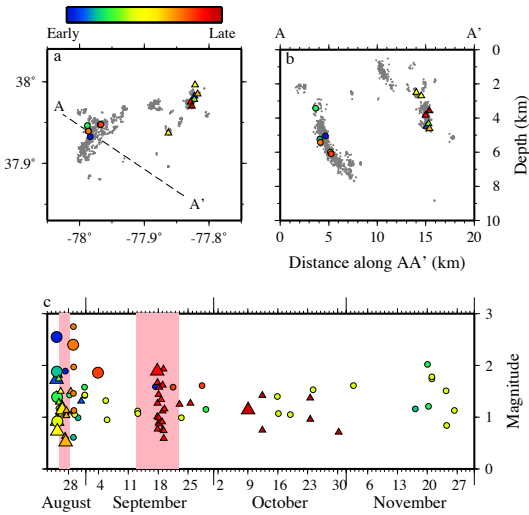


**Fig. 11.** (a) and (b) The map and cross-section view of 13 repeater families, respectively, which are color-code by the origin times of the first event in the family. Circles denote repeater families in Box A. Triangles denote repeater families in Box B. (c) Magnitude versus origin time for all repeaters. The pink shaded areas denote the time windows of two earthquake swarms.

because of the lack of geodetic instruments around the epicenter of the Virginia mainshock, afterslip could have occurred but was not observed geodetically [Roeloffs et al., 2015]. Therefore, we investigate whether the migration of earthquakes and/or repeaters occurred following the mainshock, which is often considered as manifestation of aseismic creep or afterslip [e.g., Tajima and Kanamori, 1985; Henry and Das, 2001; Peng and Zhao, 2009; Kato et al., 2012; Yao et al., 2017; Wu et al., 2017]. Repeaters are a set of events that rupture the same fault patches and produce highly similar waveforms at recording stations, while the rest fault areas overtake aseismic creep [e.g., Nadeau et al., 1995; Peng et al., 2005; Zhao and Peng, 2009].

Because the number of detected earthquakes by regional seismic stations is very small, we investigate the aftershock migration with the detected catalog starting ~1.5 days after the mainshock. First, we identify repeaters by looking for event pair with  $CC > 0.9$ . When the number of events linked by high waveform similarity

reaches 3, a repeater family is formed. 6 and 7 repeater families are identified in Box A and B, respectively (Figure 11). All repeater families started within a few days following the mainshock, except for two families in Box B (Figure 11c). There was no systematic migration pattern for the activation of repeater families (Figure 11a and b). Then, we examine the spatial-temporal evolution of all seismicity along AA', BB' and depth (Figure 11). In both Boxes, we find that the aftershock zone did not expand with time along either strike or dip. However, we note that we did not have the complete aftershock sequence within  $\sim 1.5$  days after the mainshock, during which aftershock expansion would be most significant if driven by afterslip [Peng and Zhao, 2009; Lengline et al., 2012]. Therefore, along with the absence of geodetic measurements, we also did not have sufficient evidence that afterslip did drive aftershocks on the mainshock rupture plane.

### 3.5.4 Hurricane Irene

In critically stressed tectonic settings, seismic events can be prompted or inhibited by extreme weather events (e.g., rainfall, hurricane or typhoon). For example, Hainzl et al. [2013] found that pore-fluid pressure diffusion in subsurface due to rainfall induced seismicity rate increase at Mt. Hochstaufen, Germany. Seismicity modified by atmospheric pressure changes has also been studied, but in a much less extent. Gao et al. [2000] illustrated an annual modulation of the triggered earthquake rate in California following the 1992  $M_w$  7.3 Landers earthquake by atmosphere pressure changes, which reduce the normal stress along faults and enhance seismicity.

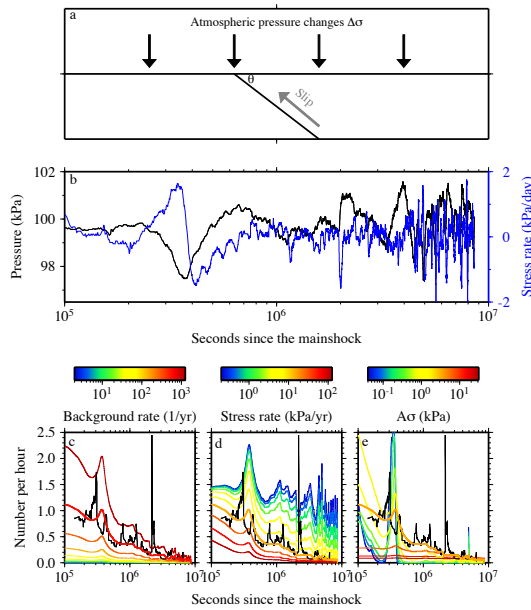


**Fig. 12.** (a) A cartoon showing how atmospheric pressure changes  $\Delta\sigma$  may affect reverse faulting with a dip angle  $\theta$ . (b) Time series of atmospheric pressure and Coulomb stress rate acting on the reverse faulting plane. (c) The smoothed seismicity rate changes in Box B (black) and predicted seismicity rate changes with  $\dot{S} = 12.8 \text{ kPa/yr}$ ,  $\Delta\sigma = 3.2 \text{ kPa}$  and varying background seismicity rate  $r$ . The thick line denotes the optimized prediction. (d) Similar to panel (c), with  $r = 512 \text{ yr}^{-1}$ ,  $\Delta\sigma = 3.2 \text{ kPa}$  and varying stress rate  $\dot{S}$ . (e) Similar to panel (c), with  $\dot{S} = 12.8 \text{ kPa/yr}$

Liu et al., [2009] suggested that some shallow slow-slip events were triggered along the Longitudinal Valley Fault in eastern Taiwan following several wet typhoons. However, a more recent study examining the same data set showed that much of the transient signals observed by borehole strain meters were associated with rain falls, rather than aseismic slip at shallow depth [Hsu et al., 2015].

A few days following the Virginia mainshock, hurricane Irene raked the east coast of United States. Between Irene's two landfalls at Cape Lookout, North Carolina, and Brigantine Island, New Jersey, it passed through the aftershock zone of the Virginia mainshock with powerful swirls of wind [Avila and Cangialosi, 2011]. The meteorological data (e.g. precipitation, temperature and atmospheric

pressure) is recorded by a National Oceanic and Atmospheric Administration (NOAA) station 03715/LKU,  $\sim 5 \text{ km}$  from the mainshock's epicenter. We do not observe any significant changes in precipitation and temperature associated with hurricane Irene. However there was a clear atmospheric pressure drop between  $\sim 3$  and  $\sim 5$  days after the mainshock, which is caused by the pass-by of Irene (Figure 12). The onset of the first swarm in Box B coincided with the onset of the atmospheric pressure drop (Figure 12a). Because the dominant faulting types in Box B are reverse [Wu et al., 2015], the

seismicity rate increase during hurricane Irene can be qualitatively explained by fault unclamping due to atmospheric pressure drop, similar to how fluid extraction might change gravitational loading and induce earthquakes [Ellsworth, 2013]. Because the absolute atmospheric pressure change is very small (i.e.,  $< 1$  kPa) at the onset of seismicity rate increase, we suspect that the stressing rate, instead of stress, is likely the controlling factor on triggering earthquakes in this case. This is consistent with a better correlation between the derivative of atmospheric pressure (a proxy for stressing rate) and seismicity rate (Figure 12c). In the rate- and state-dependent friction model for earthquake triggering, stress steps cause aftershock-like sequences, while stress rate changes cause earthquake swarms [Dieterich, 1994; Toda et al., 2002], which may be an alternative explanation of the occurrence of the first swarm in Box B.

### 3.6. Conclusion

We performed single-station matched filter detection within 10 days before the 2011 Virginia earthquake and found no foreshock activity. We also detected 1859 aftershocks from 08/25/2011 to 12/01/2011 using 27 temporary stations and then perform magnitude calibration and hypoDD relocation for all events. On-fault aftershocks (i.e., within Box A) showed typical Omori's decay, while off-fault aftershock sequence (i.e., within Box B) included two earthquake swarms. The b-value map illustrates an overall lower b-value in Box A than that in Box B. The significant spatial variability of b-values suggests that weak or highly fractured areas may exist within an overall strong intraplate crust. Finally, we conducted comprehensive studies on aftershock triggering following the Virginia mainshock, including afterslip, dynamic triggering, static triggering and hurricane pass-by. No single triggering mechanism is able to explain all features in aftershock activities. The asymmetric aftershock distribution in Box A can be best explained by focusing of radiated dynamic stresses. The static Coulomb stress changes better explain the triggering in Box B than dynamic stresses. Moreover, the first earthquake swarm in Box B may be related to the atmospheric pressure drop due to pass-by of hurricane Irene. The results suggest that it is possible to have multiple triggering mechanisms contribute to aftershock triggering, which has also been reported by a few previous studies [Daniel et al., 2008; Meng and Peng, 2014].

## 4. Comparisons of Statistical Parameters Between Induced and Tectonic Earthquake Sequences [Meng and Peng, in prep]

### 4.1 Dataset and Method

We select earthquake sequences in CEUS to investigate their statistical characteristics. Our selection criterion includes that 1) the magnitude of mainshock above 3.0; 2) good station coverage around the earthquake sequence; 3)

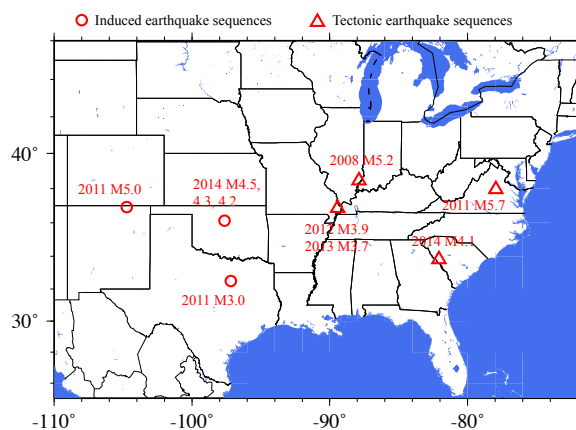


**Fig. 13.** Map of CEUS and the 10 targeted earthquake sequences. Circles and triangles denote induced and tectonic sequences, respectively.

existence of local earthquake catalogs around the origin time of mainshock. The three criteria ensure that a complete earthquake sequence can be obtained by the matched filter detection. As a result, 10 earthquake sequences are selected for further analysis (Figure 13 and Table 1). 5 out of 10 earthquake sequences are likely induced by industrial activities [Frohlich, 2012; van der Elst et al., 2013]. For the 2008 Illinois M5.2 and 2011 Colorado M5.0 sequences, the detection has already been done by Yang et al. [2009] and van der Elst et al. [2013], respectively, thus we simply use the detected catalogs from the previous studies. For the remaining 8 sequences, we perform the

matched filter detection of earthquakes within 7 days after the mainshocks, following the procedure of Meng and Peng [2016]. The templates and seismic stations distribution for the 7 sequences are shown in Figure 14. In summary, we use waveforms around the P- or S-wave of a template and cross-correlate with continuous data on all channels. Except for the templates in Oklahoma, the P- and S-wave arrivals for templates in other regions are manually picked. The correlation traces are then stacked to obtain a mean correlation trace. Correlation coefficients above a certain threshold indicate positive detections. The magnitude of the detected event is inferred as the sum of the template's magnitude and logarithmic peak amplitude ratio between the detected event and template.

**Table 1.** List of 10 earthquake sequences

Event	Mag	Type	Templates
2008 Illinois	5.2	Tectonic	Done by [Yang et al., 2009]
2011 Colorado	5.0	Induced	Done by [van der Elst et al., 2013]
2011 Texas	3.0	Induced	67 <sup>+</sup>
2011 Virginia	5.7	Tectonic	380 <sup>×</sup>
2012 New Madrid	3.9	Tectonic	1183 <sup>*</sup>
2013 New Madrid	3.7	Tectonic	1183 <sup>*</sup>
2014 S. Carolina	4.1	Tectonic	13 <sup>*</sup>
2014 Oklahoma	4.5	Induced	5379 <sup>*</sup>
2014 Oklahoma	4.3	Induced	5379 <sup>*</sup>
2014 Oklahoma	4.2	Induced	5379 <sup>*</sup>

<sup>+</sup> from Frohlich [2012];

<sup>×</sup> from McNamara et al. [2014];

<sup>\*</sup> from the ANSS catalog.

## 4.2 Results

The Frequency-Magnitude (F-M) distributions of the 10 earthquake sequences are shown in Figure 15. We fit the F-M distribution of each sequence by the Gutenberg-Richter relationship:

$$\log_{10}(N) = a - bM \quad (M > M_c)$$

using the maximum curvature method in software ZMAP [Wiemer, 2001].  $N$  is the total number of earthquakes above  $M$ , and  $M_c$  is the completeness of magnitude. For the  $M_c$  estimation, a 0.2

correction is added. The  $a$ -value indicates the total seismicity production of the sequence, which usually correlates with magnitude of the mainshock. The  $b$ -value describes the relative abundance of larger events to smaller ones, which may be negatively correlated with differential stress level [e.g., Scholz, 1968].

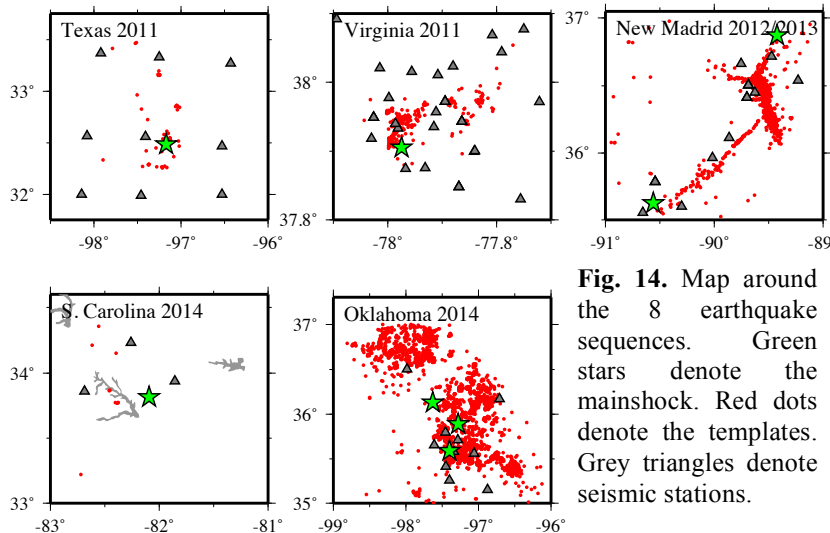


**Fig. 14.** Map around the 8 earthquake sequences. Green stars denote the mainshock. Red dots denote the templates. Grey triangles denote seismic stations.

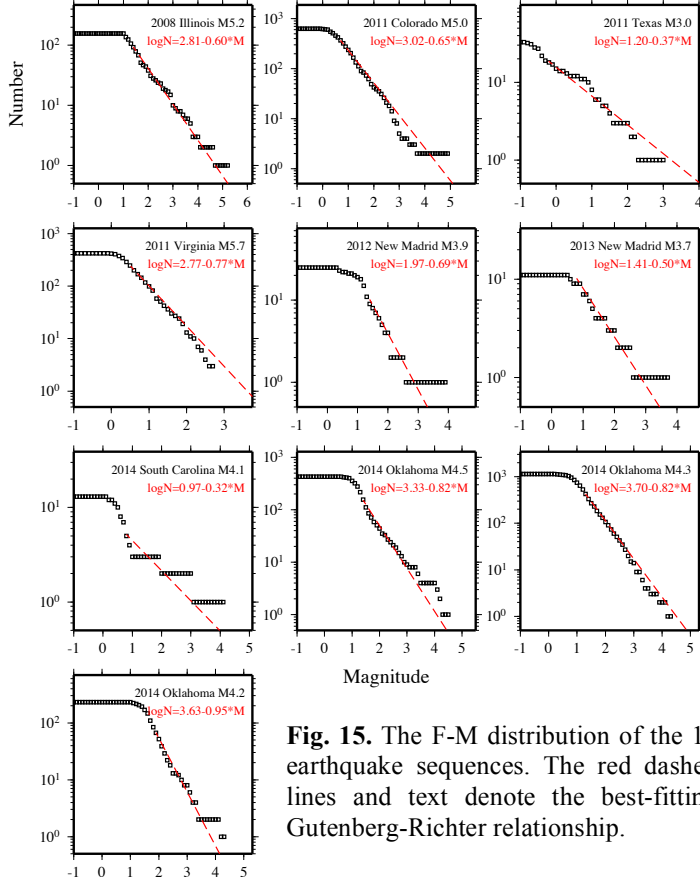


**Fig. 15.** The F-M distribution of the 10 earthquake sequences. The red dashed lines and text denote the best-fitting Gutenberg-Richter relationship.

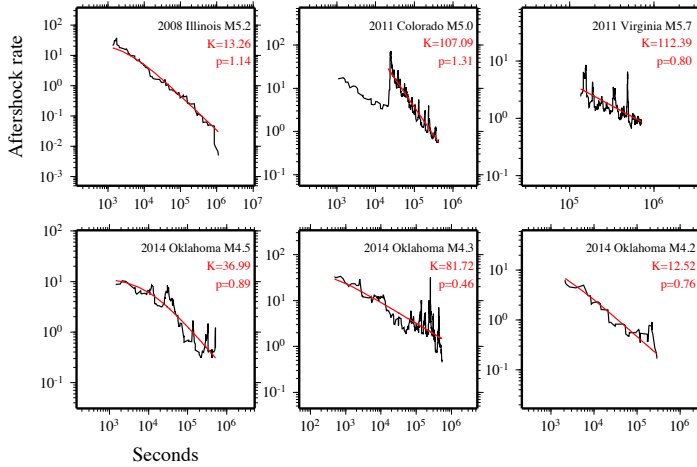


**Fig. 16.** The smoothed seismicity rate of the 6 earthquake sequences. The red lines and text denote the best-fitting modified Omori's law.

In particular, the three Oklahoma sequences have  $b$ -values higher than 0.8. The high  $b$ -values for the induced sequences suggest lower differential stress level along fault planes, which are consistent with the fluid-rich rock formation due to disposal of wastewater. The higher  $b$ -values may also indicate swarm-like sequence, which may be driven by fluid migration. Similarly, we also observe higher  $a$ -values for most induced sequences, even though they do not have the largest magnitudes. The abnormally large number of events during the induced sequences resembles earthquake swarms, that is, numerous events occur without a large mainshock.

Moreover, we compute the smoothed seismicity rate following the mainshock of each sequence with a moving window of 5 events [Ziv et al., 2003] (Figure 16). For the 4 sequences with small mainshocks (i.e., the 2011 Texas M3.0, 2012 New Madrid M3.9, 2013 New Madrid M3.7 and 2014 S. Carolina M4.1), the numbers of events are too small to compute the smoothed rate. Next, we fit the remaining 6 earthquake sequences by the modified Omori's law [Utsu et al., 1995]:

$$n(t) = \frac{K}{(t + c)^p}$$

using software AFTPOI [Ogata, 2006].  $n(t)$  is aftershock rate and  $t$  is time since the mainshock. The  $K$ -value is the productivity of the mainshock. The  $p$ -value describes the decay rate of seismicity.

Comparing the  $a$ - and  $b$ -values of the 10 earthquake sequences (Figure 17a), it appears that the tectonic sequences tend to have lower  $a$ - and  $b$ -values than the induced ones. The tectonic sequences, except the 2011 Virginia sequence, have low  $b$ -values, which are typical for intraplate earthquakes. Because of the small number of events within the 2012, 2013 New Madrid and 2014 S. Carolina sequences, the  $b$ -value measurements have much larger errors than other sequences. The relative high  $b$ -value for the 2011 Virginia sequence may be caused by an off-fault earthquake swarm [Meng et al., 2017]. The induced sequences, except the 2011 Texas sequence, have  $b$ -values above 0.65.



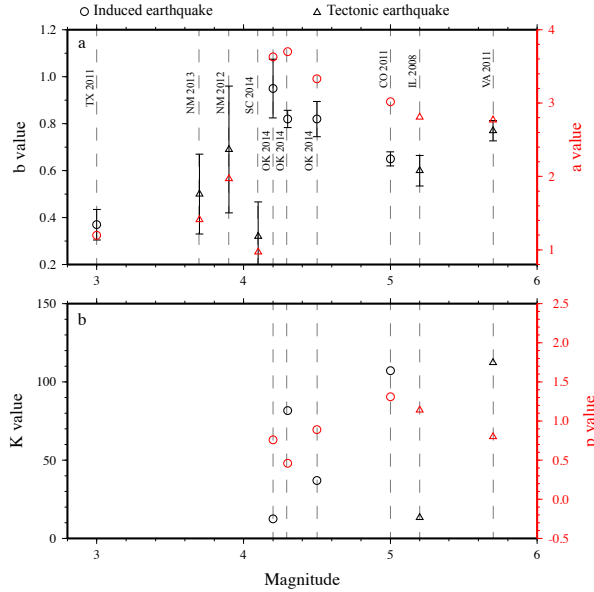


**Fig. 17.** a) The  $a$ - and  $b$ -values versus magnitude of mainshocks for the 10 earthquake sequences. b) The  $K$ - and  $p$ -values versus magnitude of mainshocks for 6 earthquake sequences.

within CEUS, which affects many parameters. For example, Meng et al. [2017] showed that  $b$ -values vary spatially within the 2011 Virginia aftershock zone. Second, different mechanisms may be responsible for the occurrence of induced earthquake sequences [Ellsworth, 2013]. If the induced sequence is driven by fluid migration, it may behave more like a swarm. If the induced sequence is triggered by shear and normal stress changes from fluid injection/extraction, it may act as a typical aftershock sequence. Finally, some statistical parameters of earthquake sequence may be heavily affected by the magnitude of mainshock (e.g.,  $a$ -value). The dependence of  $p$ -value on the trigger size is still under debate as well [Ouillon and Sornette, 2005; Hainzl and Marsan, 2008].

### Students Support

This grant supported GT graduate student Xiaofeng Meng's final thesis work on the Virginia earthquake, and a few month of postdoc before he moved on to work as a postdoc fellow at University of Washington [Meng et al., 2015, 2017a, 2017b]. It also provided partial support for GT undergraduate student (now graduate student) Clara Daniels for her work on the 2014 M4.1 earthquake near the border of SC and GA [Meng et al., 2015; Daniels et al., 2017]. Finally, it also supported PI Peng's collaboration with Professor Xiaowei Chen at University of Oklahoma on detecting microseismicity in an induced earthquake sequence in Central Oklahoma [Chen et al., 2016a,b, 2017] and remote dynamic triggering [Qin et al., 2017], and a state-wide 2D Pg tomography [Pei et al., 2017].

### Bibliography supported by this grant (\*students/postdocs mentored)

#### Manuscripts

Chen, X., T. Geobel, X. Meng\*, Z. Peng and J. Chang (2017), Temporal correlation between seismic moment and injection volume for an induced earthquake sequence in central Oklahoma, *J. Geophys. Res.*, in revision.

However, we do not find systematic differences in  $K$ - and  $p$ -values between the induced and tectonic sequences (Figure 17b). In contrast, Llenos and Michael [2013] suggested that induced sequences in Oklahoma and Arkansas may have larger  $K$ -values. The only point worthy mentioning is that the Oklahoma sequences tend to have low  $p$ -values, which indicates slower relaxation process than typical tectonic earthquake sequence.

In summary, we find that induced earthquake sequences tend to have larger  $a$ - and  $b$ -values than tectonic ones. However, we also observe significant variations for all parameters among the targeted earthquake sequences. For example, the 2011 Texas sequence, an induced sequence, has the lowest  $a$ - and  $b$ -value. Many factors may contribute to such significant variations. First of all, although the CEUS is treated as a single region in this study, stress state and material properties may vary significantly

- Pei, S. Z. Peng and X. Chen (2017), Locations of injection-induced earthquakes in Oklahoma controlled by crustal structures, *J. Geophys. Res.*, submitted.
- Meng\*, X., H. Yang\*, and Z. Peng (2017a), On-fault and Off-fault Aftershock Triggering Following the 2011  $M_w$ 5.7 Virginia Earthquake, *J. Geophys. Res.*, submitted.
- Meng\*, X., Z. Peng, and X. Chen (2017b), Statistical discrimination of induced and tectonic earthquake sequences in Central and Eastern US based on waveform detected catalogs, in prep.
- Daniels, D., Z. Peng, Q. Wu, S. Ni, X. Meng, D. Yao, L. Wagner, K. Fischer, and R. Hawman (2017), Detection of Microseismicity Surrounding the 2014  $M_w$  4.1 South Carolina Earthquake and Constraints on Depth and Stress Drop, *Seismol. Res. Lett.*, in prep.

#### Conference Abstracts

- Chen, X. Z. Peng, X. Meng, C. Chen, J. Haffener and J. Chang (2016a), Detailed analysis of an earthquake cluster potentially driven by a low-volume disposal well in central Oklahoma, *Seismo. Res. Lett.*, 87(2B), 477-478.
- Chen, X, R.E. Abercrombie, C. Pennington, X. Meng and Z. Peng (2016b), Source parameter validations using multiple-scale approaches for earthquake sequences in Oklahoma: implications for earthquake triggering processes, Abstract S13A-2515 presented at 2016 Fall Meeting, AGU, San Francisco, Calif., 12-16 Dec.
- Meng\*, X., C. Daniels\*, E. Smith\*, Z. Peng, X. Chen, L. Wagner, K. Fisher, and R. Hawman (2015), Statistical discrimination of induced and tectonic earthquake sequences in Central and Eastern US based on waveform detected catalogs, Abstract S13B-2851 presented at 2015 Fall Meeting, AGU, San Francisco, Calif., 14-18 Dec.
- Peng, Z., X. Chen, Z. Li, D. Yao, C. Zhang, X. Liu, C. Pennington, Y. Qin (2016), Monitoring seismic activities at Fairview and Woodward area in Oklahoma, Abstract S43C-2867 presented at 2016 Fall Meeting, AGU, San Francisco, Calif., 12-16 Dec.
- Qin, Y. X. Chen, Z. Peng, and C. Aiken (2017), Dynamic triggering study in Woodward, Oklahoma, abstract submitted to the Annual Seismological Society of America meeting, Denver, CO.

#### **References:**

- Atkinson, G. M. et al. Hydraulic Fracturing and Seismicity in the Western Canada Sedimentary Basin. *Seismo. Res. Lett.*, 87, 631–647 (2016).
- Avila, L. A., & Cangialosi, J. (2011). *Hurricane Irene*. Retrieved from Miami, Fla: <http://www.nhc.noaa.gov/2011atlan.shtml>
- Bao, X. and D.W. Eaton (2016), Fault activation by hydraulic fracturing in western Canada. *Science*, 354, 1406-1409.
- Chapman, M. C. (2013), On the Rupture Process of the 23 August 2011 Virginia Earthquake, *Bull. Seismo. Soc. Am.*, 103(2A), 613-628.
- Cleveland, K. M., and C. J. Ammon (2015), Precise Relative Earthquake Magnitudes from Cross Correlation, *Bulletin of the Seismological Society of America*, 105(3), 1792-1796.
- Daniel, G., Marsan, D., & Bouchon, M. (2008). Earthquake triggering in southern Iceland following the June 2000  $M_s$  6.6 doublet. *Journal of Geophysical Research-Solid Earth*, 113(B5). doi:10.1029/2007jb005107
- Dieterich, J. (1994). A Constitutive Law for Rate of Earthquake Production and Its Application to Earthquake Clustering. *Journal of Geophysical Research-Solid Earth*, 99(B2), 2601-2618. doi:10.1029/93jb02581

- Ellsworth, W. L. (2013), Injection-Induced Earthquakes, *Science*, 341(6142), 143-149.
- Frohlich, C. (2012), Two-year survey comparing earthquake activity and injection-well locations in the Barnett Shale, Texas, *P Natl Acad Sci USA*, 109(35), 13934-13938.
- Gao, S.S., P.G. Silver, A.T. Linde, and I.S. Sacks (2000), Annual modulation of triggered seismicity following the 1992 Landers earthquake in California. *Nature*, 406(6795), 500-504. doi:Doi 10.1038/35020045
- Hainzl, S., and D. Marsan (2008), Dependence of the Omori-Utsu law parameters on main shock magnitude: Observations and modeling, *J. Geophys. Res.*, 113, B10309, doi:10.1029/2007JB005492.
- Hainzl, S., Y. Ben-Zion, C. Cattania, and J. Wassermann (2013), Testing atmospheric and tidal earthquake triggering at Mt. Hochstaufen, Germany. *Journal of Geophysical Research-Solid Earth*, 118(10), 5442-5452. doi:Doi 10.1002/Jgrb.50387
- Hartzell, S., C. Mendoza, and Y. H. Zeng (2013), Rupture model of the 2011 Mineral, Virginia, earthquake from teleseismic and regional waveforms, *Geophysical Research Letters*, 40(21), 5665-5670.
- Henry, C., and S. Das (2001), Aftershock zones of large shallow earthquakes: fault dimensions, aftershock area expansion and scaling relations. *Geophysical Journal International*, 147(2), 272-293. doi: 10.1046/j.1365-246X.2001.00522.x
- Herrmann, R. B. (2011), St. Louis University Earthquake Center website, edited.
- Horton, S. (2012), Disposal of Hydrofracking Waste Fluid by Injection into Subsurface Aquifers Triggers Earthquake Swarm in Central Arkansas with Potential for Damaging Earthquake, *Seismol Res Lett*, 83(2), 250-260.
- Horton, J. W., Jr., A. K. Shah, D. E. McNamara, S. L. Snyder, and A. M. Carter (2015), Aftershocks illuminate the 2011 Mineral, Virginia, earthquake causative fault zone and nearby active faults, *The Geological Society of America Special Papers* 509.
- Lengine, O., B. Enescu, Z. Peng, and K. Shiomi (2012), Decay and migration of the early aftershock activity following the Tohoku Mw9.0 2011 earthquake, *Geophys. Res. Lett.*, 39, L18309, doi:10.1029/2012GL052797.
- Lei, X., D. Huang, J. Su, G. Jiang, X. Wang, H. Wang, X. Guo and H. Fu (2017), Fault reactivation and earthquakes with magnitudes of up to Mw4.7 induced by shale-gas hydraulic fracturing in Sichuan Basin, China, *Sci. Rep.*, 7:1971.
- Llenos, A. L., and Michael, A. J. (2013), Modeling Earthquake Rate Changes in Oklahoma and Arkansas: Possible Signatures of Induced Seismicity, *B Seismol Soc Am*, 103(5), 2850-2861.
- Lin, G. Q., and P. Shearer (2006), The COMLOC earthquake location package, *Seismological Research Letters*, 77(4), 440-444.
- Liu, C., A. Linde, and S. Sacks (2009), Slow earthquakes triggered by typhoons. *Nature*, 459(7248), 833-836. doi:10.1038/nature08042.
- Kato, A., Obara, K., Igarashi, T., Tsuruoka, H., Nakagawa, S., & Hirata, N. (2012). Propagation of Slow Slip Leading Up to the 2011 M-w 9.0 Tohoku-Oki Earthquake. *Science*, 335(6069), 705-708. doi:DOI 10.1126/science.1215141
- Keranen, K. M., M. Weingarten, G. A. Abers, B. Bekins, and S. Ge. (2014), Sharp increase in central Oklahoma seismicity since 2008 induced by massive wastewater injection, *Science*, 345, 448-451.

- McNamara, D. E., H. M. Benz, R. B. Herrmann, E. A. Bergman, P. Earle, A. Meltzer, M. Withers, and M. Chapman (2014), The Mw 5.8 Mineral, Virginia, Earthquake of August 2011 and Aftershock Sequence: Constraints on Earthquake Source Parameters and Fault Geometry, *Bull. Seismo. Soc. Am.*, 104(1), 40-54.
- Meng, X., and Z. Peng (2014), Seismicity rate changes in the Salton Sea Geothermal Field and the San Jacinto Fault Zone after the 2010 Mw7.2 El Mayor-Cucapah Earthquake, *Geophysical Journal International*, 197(2), doi: 10.1093/gji/ggu085.
- Meng, X., Z. Peng, and J. Hardebeck (2013a), Seismicity around Parkfield correlates with static shear stress changes following the 2003 Mw6.5 San Simeon earthquake, *J Geophys Res-Sol Ea*, 118(7), 3576-3591.
- Meng, X., Z. Peng, H. Yang, and S. Allman (2013b), Hurricane Irene's Impacts on the Aftershock Sequence of the 2011 Mw5.8 Virginia Earthquake, in *2013 AGU Fall meeting*, edited, San Francisco, CA.
- Meng, X. and Z. Peng (2016), Increasing lengths of aftershock zones with depths of moderate-size events on the San Jacinto Fault suggests triggering of deep creep, *Geophys. J. Int.*, 204(1), 250-261, doi:10.1093/gji/ggv445.
- Mogi, K. (1962), Magnitude frequency relations for elastic shocks accompanying fractures of various materials and some related problems in earthquakes, *Bull. Earthquakes Res. Inst. Univ. Tokyo*, 40, 831-853.
- Mogi, K. (1962), Magnitude frequency relations for elastic shocks accompanying fractures of various materials and some related problems in earthquakes, *Bull. Earthquakes Res. Inst. Univ. Tokyo*, 40, 831-853.
- Nadeau, R. M., W. Foxall, and T.V. Mcevilley (1995), Clustering and Periodic Recurrence of Microearthquakes on the San-Andreas Fault at Parkfield, California. *Science*, 267(5197), 503-507. doi:DOI 10.1126/science.267.5197.503
- Ogata, Y. (2006), Fortran programs statistical analysis of seismicity -updated version (point process data), EPTREN, LINLIN, SIMBVP, LINSIM and PGRAPH included in Time Series and Control Program Package, SASeis2006, *Computer Science Monograph*, No. 33.
- Peng, Z., and P. Zhao (2009), Migration of early aftershocks following the 2004 Parkfield earthquake, *Nature Geoscience*, 2(12), 877-881.
- Peng, Z., J. E. Vidale, C. Marone and A. Rubin (2005), Systematic variations in moment with recurrence interval of repeating aftershocks, *Geophys. Res. Lett.*, 32(15), L15301, doi: 10.1029/2005GL022626.
- Roeloffs, E., D.L. Nelms, and R.A. Sheets (2015), Widespread groundwater-level offsets caused by the Mw 5.8 Mineral, Virginia, earthquake of 23 August 2011. *The Geological Society of America Special Papers*, 509. doi:10.1130/2014.2509(07).
- Scholz, C. H. (1968), Frequency-Magnitude Relation of Microfracturing in Rock and Its Relation to Earthquakes, *Bull. Seismol. Soc. Am.*, 58(1), 399-.
- Shcherbakov, R., D.L. Turcotte, and J.B. Rundle (2005), Aftershock Statistics, *Pure. Appl. Geophys.*, 162, 1051-1076.
- Shelly, D. R., W. L. Ellsworth, and D. P. Hill (2016), Fluid-faulting evolution in high definition: Connecting fault structure and frequency-magnitude variations during the 2014 Long Valley Caldera, California, earthquake swarm, *J Geophys Res-Sol Ea*, 121(3), 1776-1795.

- Skoumal, R.J., M.R. Brudzinski, B.S. Currie (2015), Earthquakes induced by hydraulic fracturing in Poland Township, Ohio, *Bull. Seismo. Soc. Am.*, 105(1), 189-197.
- Tajima, F., and H. Kanamori (1985), Global Survey of Aftershock Area Expansion Patterns. *Physics of the Earth and Planetary Interiors*, 40(2), 77-134. doi:10.1016/0031-9201(85)90066-4
- Toda, S., R.S. Stein, G. Beroza, and D. Marsan (2012), Aftershocks halted by static stress shadows. *Nature Geoscience*, 5(6), 410-413. doi:10.1038/NGEO1465
- Tormann, T., B. Enescu, J. Woessner, and S. Wiemer (2015), Randomness of megathrust earthquakes implied by rapid stress recovery after the Japan earthquake, *Nature Geoscience*, 8(2), 152-158.
- Utsu, T., Ogata, Y., and Matsuura, R. (1995), The centenary of the Omori formula for a decay law of aftershock activity, *Journal of Physics of the Earth*, 43(1), 1-33.
- van der Elst, N.J., Savage, H.M., Keranen, K.M., and Abers, G.A. (2013), Enhanced remote 100 earthquake triggering at fluid-injection sites in the Midwestern United States, *Science*, 341(6142), 164-167.
- Waldhauser, F., and W. Ellsworth (2000), A double-difference earthquake location algorithm: Method and application to the northern Hayward fault, California, *Bulletin of the Seismological Society of America*, 90(6), 1353-1368.
- Walsh, F. R., and M. D. Zoback (2015), Oklahoma's recent earthquakes and saltwater disposal, *Science Advances*, 1(June), 1-9, doi:10.1126/sciadv.1500195.
- Weingarten, M., S. Ge, J. W. Godt, B. a. Bekins, and J. L. Rubinstein (2015), High-rate injection is associated with the increase in U.S. mid-continent seismicity, *Science*, 348(6241), 1336-1340, doi:10.1126/science.aab1345.
- Wiemer, S. (2001), A software package to analyze seismicity: ZMAP, *Seismological Research Letters*, 72, 373-382.
- Wu, J., D. Yao, X. Meng, Z. Peng, J. Su, and F. Long (2017), Spatial-temporal evolutions of early aftershocks following the 2013 Mw6.6 Lushan earthquake in Sichuan, China, *J. Geophys. Res.*, 122, 2873-2889, doi:10.1002/2016JB013706.
- Wu, Q. M., M. C. Chapman, and J. N. Beale (2015), The Aftershock Sequence of the 2011 Mineral, Virginia, Earthquake: Temporal and Spatial Distribution, Focal Mechanisms, Regional Stress, and the Role of Coulomb Stress Transfer, *Bull. Seismol. Soc. Am.*, 105(5), 2521-2537.
- Yang, H., L. P. Zhu, and R. S. Chu (2009), Fault-Plane Determination of the 18 April 2008 Mount Carmel, Illinois, Earthquake by Detecting and Relocating Aftershocks, *Bull. Seismol. Soc. Am.*, 99(6), 3413-3420.
- Yao, D., J. I. Walter, X. Meng, T. E. Hobbs, Z. Peng, A. V. Newman, S. Y. Schwartz, and M. Protti (2017), Detailed spatio-temporal evolution of microseismicity and repeating earthquakes following the 2012 Mw 7.6 Nicoya earthquake, *J. Geophys. Res.*, 122, doi:10.1002/2016JB013632.
- Zhao, P., and Z. Peng (2009), Depth extent of damage zones around the central Calaveras fault from waveform analysis of repeating earthquakes, *Geophys. J. Int.*, 179, 1817-1830, doi:10.1111/j.1365-246X.2009.04385.x.
- Ziv, A., A. M. Rubin, and D. Kilb (2003), Spatiotemporal analyses of earthquake productivity



and size distribution: Observations and simulations, Bull. Seismol. Soc. Am., 93, 2069–2081.